SAND2000-2414J

Electromagnetic induction in a fully 3D anisotropic Earth

Chester J. Weiss and Gregory A. Newman

Sandia National Laboratories, Geophysical Technology Department,

PO Box 5800 MS–0750, Albuquerque NM 87185

Abstract

The bulk electrical anisotropy of sedimentary formations is a macroscopic phenomenon which can result from the presence of sand/shale laminae and varations in grain size and pore space. Accounting for its effects on induction log response is an ongoing research problem for the well–logging community since these types of sedimentary stuctures have long been correlated with productive hydrocarbon reservoirs. Presented here is a staggered grid finite difference method for simulating EM induction in a fully 3D anisotropic medium. Here, the electrical conductivity of the formation is represented as a full 3×3 tensor whose elements can vary arbitrarily with position throughout the formation. To demonstrate the validity of this approach, finite difference results are compared against analytic and quasianalytic solutions for tractable 1D and 2D model geometries. As an final example, we simulate 2C–40 induction tool responses in a crossbedded eolian sandstone to illustrate the magnitude of the challenge faced by interpreters when electrical anisotropy is neglected.

Introduction

Determination of the electrical anisotropy of geologic formations is a problem that has attracted the attention of geophysicists for nearly 70 years (*c.f.* Maillet and Doll, 1932; Kunz and Moran, 1958). The reasons why have varied greatly, ranging from ground water investigation (Christensen, 2000), to hydrocarbon exploration (Moran and Gianzero, 1979; Anderson *et al.*, 1998; Avdeev *et al.*, 2000), to regional–scale crustal mapping (Weidelt, 1999; Everett and Constable, 1999). Some materials, such as olivine, exhibit an inherent electrical anisotropy (Constable *et al.*, 1992). However, in the studies cited above and the work presented here, the electrical anisotropy in question is regarded as a macroscopic effect arising from the presence of a

DISCLAIMER

DISCLAIMER

Portions of this document may be illegible in electronic image products. Images are produced from the best available original document.

regular sequence of alternating, "small scale" lithologic units (*e.g. sand/shale interbeds*) which are themselves isotropic in nature.

Within an eolian sand unit (figure 1), variations in the grain size and pore space geometry alter the directional mobility of electric charge carriers residing in the interstitial fluids (Klein *et al.*, 1997). This effect can hinder accurate formation evaluation when induction log measurements are interpreted in the usual manner (Moran and Kunz, 1962; Anderson *et al.*, 1998). To lend clarity to this situation, we have developed a numerical model which computes the electric and magnetic fields generated by inductive sources in a fully three–dimensional (3D) anisotropic medium. The model is based on a staggered grid finite difference (FD) solution to Maxwell's equations in the quasi–static limit.

This work differs from a previously developed FD solution (Weidelt, 1999), also designed to simulate induction in anisotropic media. Both methods incorporate the staggered grid approach: This study, an edge–based discretization; Weidelt (1999), a face–centered discretization. For the face–based discretization, the governing PDE (derived from Maxwell's equations in the quasi–static limit) is discretized using components of the electric field vector which are normal to and located at the centers of FD cell faces. However, the continuity of electric current at cell interfaces renders these components of the electric field discontinuous and requires a sophisticated averaging scheme to accomodate the effects of electrical anistropy. In contrast, the edge–based approach utilizes electric field components which are tangential to conductivity boundaries and are thus locally continuous and well-behaved. The resulting scheme for accomodating an electrically anisotropic medium is presented here and has the advantage in being simpler to implement.

The paper is organized as follows. We begin by deriving the governing partial differential equation (PDE) which describes low–frequency electromagnetic induction in anisotropic media. Next, we introduce the FD method for staggered grids used in solving the governing PDE. Incorporation of a fully generalized anisotropy tensor into the FD method is discussed at length, but a detailed derivation of the discretized current density terms is found later in the appendix. In closing the discussion of the FD method, we briefly comment on the quasi–minimal residual method used here to solve the FD linear system of equations. Lastly, we present the results of several numerical experiments. The first set of results illustrate the agreement between the FD solutions and analytic/quasi–analytic solutions in 1D and 2D model geometries. The last set of computations

illustrates the magnitude of the effect of anisotropy on a 2C–40 induction logging instrument in a fully 3D crossbedded formation.

Methodology

The governing equations for electromagnetic induction are Faraday's law,

$$\nabla \times \mathbf{E} = -i\omega\mathbf{B}, \tag{1}$$

which relates the electric field $\mathbf{E}$ to the magnetic induction $\mathbf{B}$, and Ampere's law,

$$\nabla \times \mathbf{H} = \mathbf{J}_i + \mathbf{J}_s + i\omega\mathbf{D}, \tag{2}$$

which relates the magnetic field $\mathbf{H}$ to the induced and source current densities ($\mathbf{J}_i$ and $\mathbf{J}_s$) and displacement fields $\mathbf{D}$. An $\exp(i\omega t)$ time–dependence is implicit in this formulation where ω is angular frequency.

The induction and magnetic fields are related by the constitutive relationship $\mathbf{B} = \mu\mathbf{H}$, where μ is the magnetic permeability of the medium. Similarly, the displacement and electric fields are also assumed to be linearly dependent, related by $\mathbf{D} = \epsilon\mathbf{E}$, where ϵ is the electric permittivity. Lastly, the induced current density $\mathbf{J}_i$ is assumed to be that due to purely ohmic conduction in an anisotropic medium and is written as

$$\mathbf{J}_i = \bar{\sigma}\mathbf{E}, \tag{3}$$

where $\bar{\sigma}$ is a symmetric 3×3 tensor. The symmetry of the conductivity tensor results from neglecting the effect of Hall currents produced by Earth's main magnetic field (Onsager, 1931) and is necessary for a physically sensible energy dissipation within the Earth.

In formulating the electomagnetic induction problem, we note that the electric field $\mathbf{E}$ can be expressed as the sum of a "primary" contribution $\mathbf{E}_0$ due to source currents $\mathbf{J}_s$ embedded in a background reference medium, and a "scattered" contribution $\mathbf{E}'$ arising from conductivity and permittivity variations which deviate from the background structure. That is,

$$\mathbf{E} = \mathbf{E}_0 + \mathbf{E}'. \tag{4}$$

For the computations that follow, the background electrical structure is a uniform wholespace of conductivity σ_0, permittivity ϵ_0, and free space permeability μ_0. Combining equations (1) through (4) yields a single,

2nd order PDE in terms of the scattered electric field,

$$\nabla \times \nabla \times \mathbf{E}' + i\omega\mu(\bar{\sigma} + i\omega\epsilon)\mathbf{E}' = -i\omega\mu\mathbf{J}_0. \tag{5}$$

The $\mathbf{J}_0$ term is the effective source current density for the scattered fields and is given by the expression,

$$\mathbf{J}_0 = \left[(\bar{\sigma}(\mathbf{x}) - \sigma_0\mathbf{I}) + i\omega(\epsilon(\mathbf{x}) - \epsilon_0)\mathbf{I}\right]\mathbf{E}_0, \tag{6}$$

where the spatial dependence of the conductivity and permittivity is explicitly noted by the position vector $\mathbf{x}$ and $\mathbf{I}$ is the 3×3 identity matrix. For a uniform wholespace, the background electric field $\mathbf{E}_0$ is readily computed in the low frequency limit from analytic formulae for dipolar sources (Ward and Hohmann, 1987). At frequencies up to $f = \omega/2\pi \sim 1$ MHz, this approximation is a reasonable one since the permittivity of the formation yields a negligible effect. Nonetheless, this term is retained in equations (5) and (6) for completeness and to emphasize that the approach taken here is also applicable to higher frequency problems.

The unknown fields $\mathbf{E}'$ in equation (5) are determined by the method of finite differences (FD) on a staggered "Yee" grid (Yee, 1966) where the physical domain is discretized into Cartesian cells and the scattered electric field components (E'_x, E'_y and E'_z) are defined on the edge of the cells. If necessary, magnetic fields are computed at cell faces as a postprocessing step based on a differences approximation to Faraday's Law, equation (1). Figure 2 illustrates the relationship between a cell and the computed electric field components.

Examination of figure (2) indicates that the conductivity and dielectric permittivity will be required on cell edges because that is where the electric field is sampled. In the isotropic case, following the work of Newman and Alumbaugh (1995), the average conductivity/permittivity on the cell edge can be evaluated using Ampere's Law by tracing out a line integral of the magnetic field, centered on the midpoint of the cell edge. The resulting conductivity/permittivity are simply a weighted sum of the conductivities/permittivities of the four adjoining cells, where the weighting is based on the area of each cell that is bounded by the line integral. For the anisotropy problem, however, this approach must be extended because incorporating the effects of a generalized anisotropy tensor (the $\bar{\sigma}\mathbf{E}'$ term in equation (5)) requires values of not only the $\hat{x}$–component of the scattered electric field at the point $(i + \frac{1}{2}, j, k)$ but also the $\hat{y}$– and $\hat{z}$–components at

this same point since,

$$\hat{x} \cdot \bar{\sigma}\mathbf{E}' = \sigma_{xx}E'_x + \sigma_{xy}E'_y + \sigma_{xz}E'_z. \tag{7}$$

We approximate the values of E'_y and E'_z at this point with a linear combination of their respective values at the neighboring points, as indicated by the solid arrows in figure (2).

The method by which these terms are approximated is closely linked with that used to symmetrize the FD system of linear equations. Newman and Alumbaugh (1995) noted that, for the isotropic case, the coefficient matrix of the linear system would be symmetric if each equation arising from the $\hat{x}$–component of equation (5) at $(i+\frac{1}{2}, j, k)$ was first multiplied by a scale factor $\Delta x_i(\Delta y_{j+1} + \Delta y_{j-1})(\Delta z_{k+1} + \Delta z_{k-1})/4$. A similar pair of scale factors was then found for the equations arising from the $\hat{y}$ and $\hat{z}$–components centered at points $(i, j+\frac{1}{2}, k)$ and $(i, j, k+\frac{1}{2})$, respectively. For the case of slowly varying electric fields, the symmetrization process is approximately equal to a volume integration over quadrants of the neighboring cells. Therefore, to incorporate the effects of anisotropy and retain the symmetry of the coefficient matrix, the volume integration over components of the $\bar{\sigma}\mathbf{E}'$ term is carried out explicitly while the other terms in the equation are simply scaled by the integration volume. For example, evaluating the volume integral of equation (7) over the region $\Omega : [x_i < x < x_{i+1};\ y_{j-\frac{1}{2}} < y < y_{j+\frac{1}{2}};\ z_{k-\frac{1}{2}} < z < z_{k+\frac{1}{2}}]$ results in a linear combination of 9 electric field components (see figure 2). Specifically, from equation (7) we find,

$$\begin{aligned}\int_\Omega \sigma_{xx}E'_x dV \simeq \frac{1}{4}\Delta x_i(&\Delta y_j \Delta z_k \sigma_{xx\ i\,j\,k} + \Delta y_j \Delta z_{k-1}\sigma_{xx\ i\,j\,k-1} \\ &+ \Delta y_{j-1}\Delta z_k \sigma_{xx\ i\,j-1\,k} + \Delta y_{j-1}\Delta z_{k-1}\sigma_{xx\ i\,j-1\,k-1})E'_{x\ i+\frac{1}{2}\,j\,k}.\end{aligned} \tag{9}$$

Furthermore,

$$\int_\Omega \sigma_{xy}E'_y dV \simeq \alpha_1 E_1 + \alpha_2 E_2, \tag{10a}$$

where

$$\alpha_1 = \frac{1}{8}\Delta x_i \Delta y_j(\Delta z_k \sigma_{xy\ i\,j\,k} + \Delta z_{k-1}\sigma_{xy\ i\,j\,k-1}), \tag{10b}$$

$$\alpha_2 = \frac{1}{8}\Delta x_i \Delta y_{j-1}(\Delta z_k \sigma_{xy\ i\,j-1\,k} + \Delta z_{k-1}\sigma_{xy\ i\,j-1\,k-1}), \tag{10c}$$

$$E_1 = E_{y\ i\,j+\frac{1}{2}\,k} + E_{y\ i+1\,j+\frac{1}{2}\,k} \quad \text{and} \quad E_2 = E_{y\ i\,j-\frac{1}{2}\,k} + E_{y\ i+1\,j-\frac{1}{2}\,k}. \tag{10d}$$

The expression for the remaining term in equation (7) follows in a similar fashion and is omitted here for brevity. Contained in the appendix is a full account of the integration procedure for the remaining terms in

equation (7) along with the FD equations for the y and z components of the current density $\mathbf{J}$ arising from the product $\bar{\sigma}\mathbf{E}'$ in equation (5).

We note that the choice of an "edge–centered" staggered grid instead of a "face–centered" one (Weidelt, 1999) results in comparatively simple expressions for the spatially–averaged conductivity values (equations 10b–c). In the above expression, the conductivity values are averaged arithmetically since the J_x component is continuous at the point $(i + 1/2, j, k)$. In contrast, a face–centered scheme requires a somewhat more complicated geometric averaging scheme since the normal component of the electric field is discontinuous across cell faces.

By applying the centered FD and symmetry operators to equation (5), including evaluation of elements of the conductivity tensor at cell edges (see appendix for more details), a linear system of equations is assembled,

$$\mathbf{A}\mathbf{x} = \mathbf{b}, \tag{11}$$

where $\mathbf{A}$ is the complex symmetric coefficient matrix, $\mathbf{x}$ is the vector of unknown scattered electric field components on cell edges, and $\mathbf{b}$ is the source vector containing values of $\mathbf{J}_0$ (see equation (6)) evaluated at the cell edges. For cell edges which lie on the boundary of the FD mesh, a homogeneous Dirichlet condition is applied. This linear system is efficiently solved using the iterative quasi-minimal residual (QMR) algorithm (Freund, 1992). The QMR belongs to the class of Krylov subspace methods which includes the conjugate gradient method for real matrices. Following Newman and Alumbaugh (1995), we implement a Jacobi preconditioner to improve the convergence rate of the QMR iterates. Recently however, Avdeev *et al.* (2000) demonstrated a speedup of $\sim$ 10 in wall–clock time by implementing a "low induction number" preconditioner for isotropic 3D models. Adaption of this algorithm to the anisotropic case is currently underway and will be presented in a future publication.

Examples

As a simplifying step when constructing a geologically sensible conductivity model, we choose to describe the electrical conductivity tensor in terms of its principal axes reference frame. Therefore, in sedimentary formations, for example, the tensor is compactly described as $\bar{\sigma} = \mathrm{diag}(\sigma_{\|}, \sigma_{\|}, \sigma_{\perp})$, where $\sigma_{\|}$ is the conduc-

tivity in the bed–parallel direction and $\sigma_\perp$ is the conductivity perpendicular to the bedding planes. The conductivity tensor is transformed from the principal axes reference frame to the reference frame of the model (*i.e.* the x, y and z axes) via a rotation matrix $\mathbf{R}$,

$$\bar{\sigma} = \mathbf{R}^T \mathrm{diag}(\sigma_\parallel, \sigma_\parallel, \sigma_\perp)\mathbf{R}, \tag{12}$$

where the superscript T denotes the transpose operator. The elements of the rotation matrix $\mathbf{R}$ are given by the direction cosines between the principal axes and the model reference frame. For the case presented here where the conductivity in two of the three principal axes directions is equal, each of the six direction cosines are uniquely expressed in terms of only two angles corresponding to the strike ϕ and dip θ of the laminations (figure 3). This brings the total number of unknowns for each model cell in figure (2) to four: $\sigma_\perp$, $\sigma_\parallel$, θ and ϕ. In the specific case the rotation matrix takes the form,

$$\mathbf{R}^T = \begin{pmatrix} \cos\theta\cos\phi & \sin\phi & \sin\theta\cos\phi \\ -\cos\theta\sin\phi & \cos\phi & -\sin\theta\sin\phi \\ -\sin\theta & 0 & \cos\theta \end{pmatrix} \tag{13}$$

Note that the orientation of the principal axes, and therefore the values within the rotation matrix in equations (12) and (13), can vary as a function of position within the conducting formation.

To demonstrate the validity of the FD scheme developed in the previous section, we first present results of comparisons with known analytic and quasi–analytic solutions. The first example (figure 4) illustrates the agreement between the FD solution and the analytic solution for the case of a vertical magnetic dipole embedded in an anisotropic wholespace, where $\sigma_\perp$ is the conductivity in the vertical direction. This is a limiting case in which anisotropic effects are not realized by the source configuration; it serves as a baseline for assessing the accuracy of the FD code in the isotropic limit. The second example used to illustrate the accuracy of the code is taken from Avdeev *et al.* (2000) in which an array induction tool is situated in a 45° dipping conducting borehole in an anisotropic formation (figure 5). Again, the value of $\sigma_\perp$ describes the conductivity of the surrounding formation in the vertical direction. Results from the FD method and a Neumann series method (figure 6) show strong agreement for the fields computed along the receiver array. As expected, the effects of the conducting borehole diminish with increasing distance from the transmitting coil. Lastly, we conduct a self consistency check with the FD solutions to verify that the computed fields are invariant under rotations of the principal axes of the conductivity tensor. Two models (figure 7) were

constucted. In Model I the value $\sigma_\perp$ specifies the conductivity in the vertical direction (as in the previous example) and the formation is excited by a 45° dipping array induction tool. In Model II, the array induction tool is oriented vertically and the principle axes of the formation are rotated 45° in the $x - z$ plane. For each of these two models, the array is oriented 45° with respect to the prinipal axes, and thus, should measure equivalent signals. Results of this last comparison among only FD solutions are shown in figure 8 and demonstrate an acceptable agreement.

As an example of an application of our FD anisotropy model, we consider the case of a borehole induction tool in a crossbedded sandstone unit. Eolian–deposited crossbedded sands have long been identified as candidate reservoir rocks (*e.g.* the Jurassic Norphlet SS and Permian Rotliegendes SS) and remain targets for hydrocarbon exploration. The modeling results presented here simulate the reponse of a 2C-40 borehole induction tool in a brine–saturated sandstone across a bed–boundary and demonstrate the effects of electrical anisotropy on the apparent conductivity curves inferred from this instrument.

Two classes of sedimentary structures were evaluated with the modeling software: symmetrically dipping herringbone crossbeds and asymmetrically dipping crossbeds. Figure 9 illustrates the geometric configuration for the symmetrically dipping case where the borehole axis intersects the bed boundary at 90°. We note that this is not a limitation of the modeling software, but rather a restriction placed on the model to better understand the effects of the formation anisotropy. For each of the models we set the conductivity values $\sigma_\perp = 0.1$ S/m and $\sigma_\parallel = 1.0$ S/m to simulate the conductivity of a brine–saturated sand unit. The high conductivity ratio of 1:10 is consistent with that seen in clean sands (Klein *et al.*, 1997). The FD method can incorporate the effects of the borehole in the tool response. However, to isolate the effects of formation anisotropy, the conductivity of the borehole and drilling mud were not included in the simulations.

Shown in figures (10) and (11) are the simulated apparent resistivity curves as the 2C–40 tool traverses a bed boundary in the brine–saturated sand. The 2C–40 induction tool is a coaxial loop system oriented parallel to the borehole axis with a 40in transmitter–receiver coil separation and 20 kHz transmitter frequency. Owing to the high conductivity of the formation, the apparent resistivity curves were "skin–effect boosted" according to standard industry practice. Simply stated, the process incorporates higher–order terms into the approximate mapping between apparent resistivity and receiver signal strength (Moran and Kunz, 1962).

Furthermore, the curves in figures (10) and (11) were also corrected for formation dip θ. Knowledge of bedding orientation can be obtained, for example, by a conventional dip meter. Correction for formation dip in the logs shown here is achieved by a scaling factor of $1/\cos(\theta)$. This is in accordance with Moran and Gianzero's (1979) formula for the apparent conductivity,

$$\sigma_a = \sigma_\perp \lambda \sqrt{\lambda^2 \cos^2\theta + \sin^2\theta}, \tag{14}$$

where $\lambda^2 = \sigma_\parallel/\sigma_\perp$. For the case of large values of λ, as we have here ($\lambda^2 = 10$), a simple cosine correction yields acceptable results as evidenced by the apparent resistivity values far from the bed boundary in figures (10) and (11) where $\sigma_a \sim \sigma_\parallel = 1.0$ S/m.

These examples demonstrate the effects of electrical anisotropy on apparent conductivity curves through hydrocarbon reservoirs of eolian origin. Figures (10) and (11) show that for a simple 2C–40 induction tool, the bed boundary in crossbedded sandstones can give rise to a complicated pattern of apparent conductivity values that is difficult to interpret accurately with an isotropic model. These results underline the challenge faced by well log analysts when interpreting anisotropic formatinons and are consistent with the general findings of other recent modeling efforts (*e.g.* Anderson *et al.*, 1998).

Conclusions

In summary, the algorithm presented here for modeling EM induction in an aniostropic medium represents a significant improvement in the ability to accurately simulate the effects geologic structures on induction tool response. The FD method is used to solve the governing PDE which yields a complex symmetric system of linear equations. These are efficiently solved using fast, Krylov subspace methods. The geologic models which can be evaluated are fully generalized, and contain an arbitrary assemblage of 3D heterogeneities and complexities within the anisotropy tensor and can include the well bore.

Acknowledgements

The authors extend thanks to the Department of Energy's Natural Gas and Oil Technology Partnership and our industry collaborators for continued support of this project: Baker Hughes, Chevron, Electromagnetic Instruments Inc., Exxon–Mobil, Halliburton Energy Services, Pathfinder and Schlumberger. This work

was supported by the United States Department of Energy under Contract DE–AC04–94AL85000. Sandia is a multiprogram laboratory operated by Sandia Corporation, a Lockheed Martin Company, for the United States Department of Energy.

References

Anderson, B.I., Barber, T. D., and Gianzero, S. C., 1998, The effect of crossbedding anisotropy on induction tool response: 39th SPWLA Logging Symposium, Expanded Abstract, Paper B.

Avdeev, D. B., Kuvshinov, A. V., Pankratov, O. V., Newman, G. A., and Alumbaugh, D. L., 2000, Modeling induction log responses in deviated boreholes with anisotropic bedding: Geophys. (submitted).

Christensen, N. B., 2000, Difficulties in determining electrical anisotropy in subsurface investigations: Geophys. Prosp., **48** 1-19.

Constable, S., Shankland, T. J., and Duba, A., 1992, The electrical conductivity of an isotropic olivine mantle: J. Geophys. Res., **97**, 3397–3404.

Everett, M. E., and Constable, S., 1999, Electric dipole fields over an anisotropic seafloor: theory and application to the structure of 40 Ma Pacific Ocean lithosphere: Geophys. J. Int., **136**, 41-56.

Freund, R. W., 1992, Conjugate gradient-type methods for linear systems with complex symmetric coefficient matrices: SIAM J. Sci. Stat. Comput., **13**, 425-448.

Klein, J. D., Martin, P. R., and Allen, D. F., 1997, The petrophysics of electrically anisotropic reservoirs: Log Analyst, **38**, 25-36.

Kunz, K. S., and Moran, J. H., 1958, Some effects of formation anisotropy on resistivity measurements in boreholes: Geophysics, **23**, 770-794.

Maillet, R., and Doll, H. G., 1932, Théorème relatif aux millieux electriquement anisotropes et ses applications à la prospection electrique en courant continu: Erganzungshefte für Angewandte Geophysik, **3**, 109–124.

Moran, J. H., and Gianzero, S., 1979, Effects of formation anisotropy on resistivity-logging measurements: Geophysics, 44, 1266-1286.

Moran, J. H. and Kunz, K. S., 1962, Basic theory of induction logging and application to study of two-coil sondes: Geophysics, **27**, 829-858.

Newman, G. A., and Alumbaugh, D. L., 1995, Frequency-domain modelling of airborne electromagnetic responces using staggered finite differences: Geophys. Prosp., **43**, 1021-1042.

Onsager, L., 1931, Reciprocal relations in irreversible processes. I.: Phys. Rev., **37**, 405-426.

Ward, S. H. and Hohmann, G. W., 1987, Electromagnetic theory for geophysical applications, *in* Nabinghian, M., Ed., Electromagnetic Methods in Applied Geophysics, Volume 1, Theory: Soc. Expl. Geophys., 131–311.

Weidelt, P., 1999, Three–dimensional conductivity models: implications for electrical anisotropy, *in* Oristaglio, M. and Spies, B., Eds., Three–dimensional Electromagnetics: Soc. Expl. Geophys., 119–137.

Yee, K. S., 1966, Numerical solution of initial boundary value problems involving Maxwell's equations in isotropic media: IEEE Trans. Ant. Prop., **14**, 302-307.

Appendix

To begin with, we point out that the staggered FD representation of equation (5) for the x-component of the scattered electric field evaluated at point $(i+1/2, j, k)$ is given by,

$$\begin{aligned}
&\big[(E'_{y\,i+1\,j+1/2\,k} - E'_{y\,i\,j+1/2\,k})/\Delta x_i - (E'_{x\,i+1/2\,j+1\,k} - E'_{x\,i+1/2\,j\,k})/\Delta y_j \\
&\qquad - \ (E'_{y\,i+1\,j-1/2\,k} - E'_{y\,i\,j-1/2\,k})/\Delta x_i + (E'_{x\,i+1/2\,j\,k} - E'_{x\,i+1/2\,j-1\,k})/\Delta y_{j-1}\big]\Delta\overline{y_j} \\
+ \ &\big[(E'_{z\,i+1\,j\,k+1/2} - E'_{z\,i\,j\,k+1/2})/\Delta x_i - (E'_{x\,i+1/2\,j\,k+1} - E'_{x\,i+1/2\,j\,k})/\Delta z_k \\
&\qquad - \ (E'_{z\,i+1\,j\,k-1/2} - E'_{z\,i\,j\,k-1/2})/\Delta x_i + (E'_{x\,i+1/2\,j\,k} - E'_{x\,i+1/2\,j\,k-1})/\Delta z_{k-1}\big]\Delta\overline{z_k} \\
&\quad + \ i\omega\mu J_{x\,i+1/2\,j\,k} \ + \ i\omega\mu\epsilon E'_{x\,i+1/2\,j\,k} \ = \ -i\omega\mu J_{0\,x\,i+1/2\,j\,k},
\end{aligned} \tag{A.1}$$

where J_x is the x–component of the anisotropic current density given by the quantity $\hat{x}\cdot\bar{\sigma}\mathbf{E}'$, $J_{0\,x}$ is the x–component of the effective source current density given by equation (6), and internodal spacings $\Delta\overline{y_j}$ and $\Delta\overline{z_k}$ are given by $(y_{j+1}-y_{j-1})/2$ and $(z_{k+1}-z_{k-1})/2$, respectively. Similarly, we define $\Delta\overline{x_i} = (x_{i+1}-x_{i-1})/2$ and, thus, the FD equations for the y and z components at points $(i, j+1/2, k)$ and $(i, j, k+1/2)$ are given by,

$$\begin{aligned}
&\big[(E'_{z\,i\,j+1\,k+1/2} - E'_{z\,i\,j\,k+1/2})/\Delta y_j - (E'_{y\,i\,j+1/2\,k+1} - E'_{y\,i\,j+1/2\,k})/\Delta z_k \\
&\qquad - \ (E'_{z\,i\,j+1\,k-1/2} - E'_{z\,i\,j\,k-1/2})/\Delta y_j + (E'_{y\,i\,j+1/2\,k} - E'_{y\,i\,j+1/2\,k-1})/\Delta z_{k-1}\big]\Delta\overline{z_k} \\
+ \ &\big[(E'_{x\,i+1/2\,j+1\,k} - E'_{x\,i+1/2\,j\,k})/\Delta y_j - (E'_{y\,i+1\,j+1/2\,k} - E'_{y\,i\,j+1/2\,k})/\Delta x_i \\
&\qquad - \ (E'_{x\,i-1/2\,j+1\,k} - E'_{x\,i-1/2\,j\,k})/\Delta y_j + (E'_{y\,i\,j+1/2\,k} - E'_{y\,i-1\,j+1/2\,k})/\Delta x_{i-1}\big]\Delta\overline{x_i} \\
&\quad + \ i\omega\mu J_{y\,i\,j+1/2\,k} \ + \ i\omega\mu\epsilon E'_{y\,i\,j+1/2\,k} \ = \ -i\omega\mu J_{0\,y\,i\,j+1/2\,j\,k}
\end{aligned} \tag{A.2}$$

and

$$\begin{aligned}
&\big[(E'_{x\,i+1/2\,j\,k+1} - E'_{x\,i+1/2\,j\,k})/\Delta z_k - (E'_{z\,i+1\,j\,k+1/2} - E'_{z\,i\,j\,k+1/2})/\Delta x_i \\
&\qquad - \ (E'_{x\,i-1/2\,j\,k+1} - E'_{x\,i-1/2\,j\,k})/\Delta z_k + (E'_{z\,i\,j\,k+1/2} - E'_{z\,i-1\,j\,k+1/2})/\Delta x_{i-1}\big]\Delta\overline{x_i} \\
+ \ &\big[(E'_{y\,i\,j+1/2\,k+1} - E'_{y\,i\,j+1/2\,k})/\Delta z_k - (E'_{z\,i\,j+1\,k+1/2} - E'_{z\,i\,j\,k+1/2})/\Delta y_j \\
&\qquad - \ (E'_{y\,i\,j-1/2\,k+1} - E'_{y\,i\,j-1/2\,k})/\Delta z_k + (E'_{z\,i\,j\,k+1/2} - E'_{z\,i\,j-1\,k+1/2})/\Delta y_{j-1}\big]\Delta\overline{y_j} \\
&\quad + \ i\omega\mu J_{z\,i\,j\,k+1/2} \ + \ i\omega\mu\epsilon E'_{z\,i\,j\,k+1/2} \ = \ -i\omega\mu J_{0\,z\,i\,j\,k+1/2}.
\end{aligned} \tag{A.3}$$

As noted earlier in the text, the method for incorporating electrical anisotropy into the FD equations is closely linked to the method by which the FD equations were first symmetrized for the isotropic case

(Newman and Alumbaugh, 1995). To summarize their approach for the isotropic case, the linear system of FD equations was made symmetric by scaling each of the equations arising from the $\hat{x}$–component of the governing PDE (equation (A.1)) by a "volume" scale factor, Ω_x, the $\hat{y}$–component by Ω_y and the $\hat{z}$–component by Ω_z. The scale factors are equivalent to one fourth of the total volume of any four cells which share a common edge. In determining the scale factor Ω_x, the common edge is the line segment extending from $x_i < x < x_{i+1}$, which includes the point $i + \frac{1}{2}$, and its value is given by $\Delta x_i \, \Delta \overline{y}_j \, \Delta \overline{z}_k$. For the other two scale factors, Ω_y and Ω_z, their values are given by $\Delta \overline{x}_i \, \Delta y_j \, \Delta \overline{z}_k$ and $\Delta \overline{x}_i \, \Delta \overline{y}_j \, \Delta z_k$ respectively. This scaling process is approximately equivalent to an integration over the correponding volumes.

To summarize the new approach for anisotropic media, terms in the FD equations (A.1 through A.3) *not* dependent on the anisotropy tensor are scaled as before with simple multiplication by the corresponding factor, Ω_x, Ω_y or Ω_z. Terms which arise from the discretization of the current density J_x, J_y and J_z, are scaled by a more careful integration over the scaling "volume". In the discussion that follows, we demonstrate how these integrals are evaluated to incorporate a symmetric conductivity tensor $\bar{\sigma}$ into a symmetric FD system of equations.

We begin by focusing our attention on the x–component of the current density (J_x) arising from the tensor product $\bar{\sigma}\mathbf{E}'$ in equation (5). Applying the usual scaling factor to this term is approximately equal to the integration

$$J_{x\, i+\frac{1}{2}\, j\, k} \Delta x_i \, \Delta \overline{y_j} \, \Delta \overline{z_k} \quad \simeq \quad \int_{\Omega_x} J_x \, dV, \tag{A.4}$$

where Ω_x is the volume such that $x_i < x < x_{i+1}$, $y_{j-1/2} < y < y_{j+1/2}$ and $z_{k-1/2} < z < z_{k+1/2}$. In consulting figure 2, however, we note that only the x–component of the electric field is defined at the point $(i+1/2, j, k)$ on the FD staggered grid. In the most general case, computation of the current density at this point also requires estimates of the y and z–components of the electric field since $J_x = \sigma_{xx} E'_x + \sigma_{xy} E'_y + \sigma_{xz} E'_z$. To accommodate this apparent shortcoming of the staggered grid, the volume integral in equation (A.1) can be decomposed into the sum of three intregrals, each involving only one component of the electric field.

$$\int_{\Omega_x} J_x \, dV \quad \simeq \quad \int_{\Omega_x} \sigma_{xx} \, E'_x \, dV \quad + \quad \int_{\Omega_x} \sigma_{xy} \, E'_y \, dV \quad + \quad \int_{\Omega_x} \sigma_{xz} \, E'_z \, dV. \tag{A.5}$$

At this stage we recognize that the first of these integrals is easily approximated by multiplication by the

usual scaling factor. As for the other two, a reasonable approximation arises when examining the boundary conditions on the fields required by the physics of the problem.

Consider four conducting cells arranged as shown in figure 2. Assuming that the electric field is defined throughout this volume (and not just at the edges as we've done for the FD approximation), it is clear that the E_x component is also everywhere continuous since it is tangent to any possible jumps in conductivity along cell boundaries. This is not the case for the other two components, E_y and E_z. Conductivity jumps in the vertical direction necessitate a discontinuity in the E_z component along the vertical direction. Similarly, lateral conductivity jumps necessitate a discontinuity in the E_y component along the same lateral direction.

To accurately represent the possible discontinuities in the E_y and E_z fields, the remaining two volume integrals from the FD approximation in equation (A.5) are evaluated in the following manner.

$$\begin{aligned} \int_{\Omega_x} J_x \, dV \quad &\simeq \quad \Delta x_i \, \Delta \overline{y}_j \, \Delta \overline{z}_k \, \widetilde{\sigma}_{xx\, i+\frac{1}{2}\, j\, k} \, E'_{x\, i+\frac{1}{2}\, j\, k} \\ &+ \quad \Delta x_i \Delta \overline{z}_k \int_{-\frac{1}{2}\Delta y_{j-1}}^{\frac{1}{2}\Delta y_{j-1}} \sigma_{xy} \, E'_y \, dy \quad + \quad \Delta x_i \Delta \overline{y}_j \int_{-\frac{1}{2}\Delta z_{k-1}}^{\frac{1}{2}\Delta z_{k-1}} \sigma_{xz} \, E'_z \, dz, \end{aligned} \tag{A.6}$$

where the local coordinate transformation is implicit in the integration variable and the value $\widetilde{\sigma}_{xx}$ is the volume weighted average of the σ_{xx} for the four cells. The first integral in equation (A.6) is split into two in order to accommodate the discontinuity in Ey as follows,

$$\begin{aligned} \int_{-\frac{1}{2}\Delta y_{j-1}}^{\frac{1}{2}\Delta y_{j-1}} \sigma_{xy} \, E'_y \, dy \quad &= \quad \int_{-\frac{1}{2}\Delta y_{j-1}}^{0} \sigma^-_{xy} \, E'^-_y \, dy \quad + \quad \int_0^{\frac{1}{2}\Delta y_{j-1}} \sigma^+_{xy} \, E'^+_y \, dy \\ &\simeq \quad \frac{1}{2}\Delta y_{j-1} \widetilde{\sigma}^-_{xy} \, \widetilde{E}'^-_y \quad + \quad \frac{1}{2}\Delta y_j \widetilde{\sigma}^+_{xy} \, \widetilde{E}'^+_y. \end{aligned} \tag{A.7}$$

The second integral in equation (A.6) is then written as,

$$\begin{aligned} \int_{-\frac{1}{2}\Delta z_{k-1}}^{\frac{1}{2}\Delta z_{k-1}} \sigma_{xz} \, E_z \, dw \quad &= \quad \int_{-\frac{1}{2}\Delta z_{k-1}}^{0} \sigma^-_{xz} \, E'^-_z \, dz \quad + \quad \int_0^{\frac{1}{2}\Delta z_{k-1}} \sigma^+_{xz} \, E'^+_z \, dz \\ &\simeq \quad \frac{1}{2}\Delta z_{k-1} \widetilde{\sigma}^-_{xz} \, \widetilde{E}'^-_z \quad + \quad \frac{1}{2}\Delta z_k \widetilde{\sigma}^+_{xz} \, \widetilde{E}'^+_z, \end{aligned} \tag{A.8}$$

where

$$\widetilde{\sigma}^-_{xy} = \frac{1}{2}(\Delta z_k \sigma_{xy\, i\, j-1\, k} + \Delta z_{k-1} \sigma_{xy\, i\, j-1\, k-1}) / \Delta \overline{z}_k, \tag{A.9}$$

$$\widetilde{\sigma}^+_{xy} = \frac{1}{2}(\Delta z_k \sigma_{xy\, i\, j\, k} + \Delta z_{k-1} \sigma_{xy\, i\, j\, k-1}) / \Delta \overline{z}_k, \tag{A.10}$$

$$\widetilde{\sigma}^-_{xz} = \frac{1}{2}(\Delta y_j \sigma_{xz\, i\, j\, k-1} + \Delta y_{j-1} \sigma_{xz\, i\, j-1\, k-1}) / \Delta \overline{y}_j \tag{A.11}$$

and

$$\widetilde{\sigma}_{xz}^{+} = \frac{1}{2}(\Delta y_j \sigma_{xz\,i\,j\,k} + \Delta y_{j-1}\sigma_{xz\,i\,j-1\,k})/\Delta\overline{y}_j. \tag{A.12}$$

Furthermore,

$$\widetilde{E}_y^{\prime -} = \frac{1}{2}(E_{y\,i\,j-\frac{1}{2}\,k} + E_{y\,i+1\,j-\frac{1}{2}\,k}) \quad \text{and} \quad \widetilde{E}_y^{\prime +} = \frac{1}{2}(E_{y\,i\,j+\frac{1}{2}\,k} + E_{i+1\,j+\frac{1}{2}\,k}) \tag{A.13}$$

and

$$\widetilde{E}_z^{\prime -} = \frac{1}{2}(E_{z\,i\,j\,k-\frac{1}{2}} + E_{z\,i+1\,j\,k-\frac{1}{2}}) \quad \text{and} \quad \widetilde{E}_z^{\prime +} = \frac{1}{2}(E_{z\,i\,j\,k+\frac{1}{2}} + E_{z\,i+1\,j\,k+\frac{1}{2}}). \tag{A.14}$$

To complete the FD system of equations, a similar procedure is applied to the J_y components at points $(i, j{+}1/2)$ and the J_z components at points $(i, j, k{+}1/2)$ The mathematics is straighforward and not presented here in detail since the previous development serves as an adequate template. The final expressions for all symmetrized components J_x, J_y and J_z in equations (A.1-A.3) are as follows:

$$\begin{aligned}
\int_{\Omega_x} J_x\,dV \;\simeq\; & \frac{1}{4}\Delta x_i(\Delta y_j \Delta z_k \sigma_{xx\,i\,j\,k} \;+\; \Delta y_j \Delta z_{k-1}\sigma_{xx\,i\,j\,k-1} \\
& \qquad + \;\Delta y_{j-1}\Delta z_k \sigma_{xx\,i\,j-1\,k} \;+\; \Delta y_{j-1}\Delta z_{k-1}\sigma_{xx\,i\,j-1\,k-1})E'_{x\,i+\frac{1}{2}\,j\,k} \\
& + \;\frac{1}{8}\Delta x_i \Delta y_{j-1}(\Delta z_{k-1}\sigma_{xy\,i\,j-1\,k-1} + \Delta z_k \sigma_{xy\,i\,j-1\,k})(E'_{y\,i\,j-\frac{1}{2}\,k} + E'_{y\,i+1\,j-\frac{1}{2}\,k}) \\
& + \;\frac{1}{8}\Delta x_i \Delta y_j(\Delta z_{k-1}\sigma_{xy\,i\,j\,k-1} + \Delta z_k \sigma_{xy\,i\,j\,k})(E'_{y\,i\,j+\frac{1}{2}\,k} + E'_{y\,i+1\,j+\frac{1}{2}\,k}) \\
& + \;\frac{1}{8}\Delta x_i \Delta z_{k-1}(\Delta y_{j-1}\sigma_{xz\,i\,j-1\,k-1} + \Delta y_j \sigma_{xz\,i\,j\,k-1})(E'_{z\,i\,j\,k-\frac{1}{2}} + E'_{z\,i+1\,j\,k-\frac{1}{2}}) \\
& + \;\frac{1}{8}\Delta x_i \Delta z_k(\Delta y_{j-1}\sigma_{xz\,i\,j-1\,k} + \Delta y_j \sigma_{xz\,i\,j\,k})(E'_{z\,i\,j\,k+\frac{1}{2}} + E'_{z\,i+1\,j\,k+\frac{1}{2}});
\end{aligned} \tag{A.15}$$

$$\begin{aligned}
\int_{\Omega_y} J_y\,dV \;\simeq\; & \frac{1}{4}\Delta y_j(\Delta x_{i-1}\Delta z_{k-1}\sigma_{yy\,i-1\,j\,k-1} \;+\; \Delta x_{i-1}\Delta z_k \sigma_{yy\,i-1\,j\,k} \\
& \qquad + \;\Delta x_i \Delta z_{k-1}\sigma_{yy\,i\,j\,k-1} \;+\; \Delta x_i \Delta z_k \sigma_{yy\,i\,j\,k})E'_{y\,i\,j+\frac{1}{2}\,k} \\
& + \;\frac{1}{8}\Delta x_{i-1}\Delta y_j(\Delta z_{k-1}\sigma_{xy\,i-1\,j\,k-1} + \Delta z_k \sigma_{xy\,i-1\,j\,k})(E'_{x\,i-\frac{1}{2}\,j\,k} + E'_{x\,i-\frac{1}{2}\,j+1\,k}) \\
& + \;\frac{1}{8}\Delta x_i \Delta y_j(\Delta z_{k-1}\sigma_{xy\,i\,j\,k-1} + \Delta z_k \sigma_{xy\,i\,j\,k})(E'_{x\,i+\frac{1}{2}\,j\,k} + E'_{x\,i+\frac{1}{2}\,j+1\,k}) \\
& + \;\frac{1}{8}\Delta y_j \Delta z_{k-1}(\Delta x_{i-1}\sigma_{yz\,i-1\,j\,k-1} + \Delta x_i \sigma_{yz\,i\,j\,k-1})(E'_{z\,i\,j\,k-\frac{1}{2}} + E'_{z\,i\,j+1\,k-\frac{1}{2}}) \\
& + \;\frac{1}{8}\Delta y_j \Delta z_k(\Delta x_{i-1}\sigma_{yz\,i-1\,j\,k} + \Delta x_i \sigma_{yz\,i\,j\,k})(E'_{z\,i\,j\,k+\frac{1}{2}} + E'_{z\,i\,j+1\,k+\frac{1}{2}});
\end{aligned} \tag{A.16}$$

and

$$\begin{aligned}
\int_{\Omega_z} J_z\, dV \;\simeq\; & \frac{1}{4}\Delta z_k(\Delta x_{i-1}\Delta y_{j-1}\sigma_{zz\,i-1\,j-1\,k} \;+\; \Delta x_{i-1}\Delta y_j\sigma_{zz\,i-1\,j\,k} \\
& \qquad +\; \Delta x_i\Delta y_{j-1}\sigma_{zz\,i\,j-1\,k} \;+\; \Delta x_i\Delta y_j\sigma_{zz\,i\,j\,k})E'_{z\,i\,j\,k+\frac{1}{2}} \\
& +\; \frac{1}{8}\Delta x_{i-1}\Delta z_k(\Delta y_{j-1}\sigma_{xz\,i-1\,j-1\,k} + \Delta y_j\sigma_{xz\,i-1\,j\,k})(E'_{x\,i-\frac{1}{2}\,j\,k} + E'_{x\,i-\frac{1}{2}\,j+1\,k}) \\
& \quad +\; \frac{1}{8}\Delta x_i\Delta z_k(\Delta y_{j-1}\sigma_{xz\,i\,j-1\,k} + \Delta y_j\sigma_{xz\,i\,j\,k})(E'_{x\,i+\frac{1}{2}\,j\,k} + E'_{x\,i+\frac{1}{2}\,j+1\,k}) \\
& +\; \frac{1}{8}\Delta y_{j-1}\Delta z_k(\Delta x_{i-1}\sigma_{yz\,i-1\,j-1\,k} + \Delta x_i\sigma_{yz\,i\,j-1\,k})(E'_{y\,i\,j-\frac{1}{2}\,k} + E'_{y\,i\,j-\frac{1}{2}\,k+1}) \\
& \quad +\; \frac{1}{8}\Delta y_j\Delta z_k(\Delta x_{i-1}\sigma_{yz\,i-1\,j\,k} + \Delta x_i\sigma_{yz\,i\,j-1\,k})(E'_{y\,i\,j+\frac{1}{2}\,k} + E'_{y\,i\,j+\frac{1}{2}\,k+1}).
\end{aligned} \tag{A.17}$$

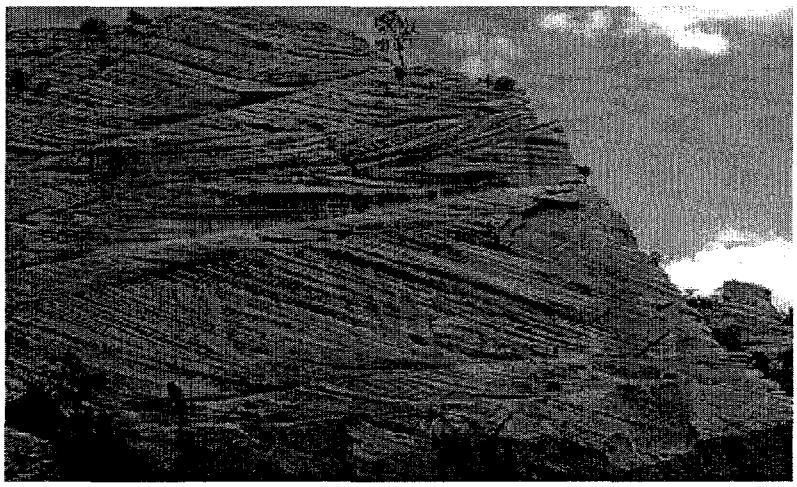

Figure 1. Crossbedded eolian deposits in the Jurassic Navajo Sandstone from Zion National Park, UT. Macroscopic electrical anisotropy in this formation results from small–scale variations in grain size and pore space which also give rise to the differential weathering shown here. This formation is analagous to the Permian Rotliegendes and Jurassic Norphlet sandstones, classic reservoirs of the North Sea and Gulf Coast, respectively. Photo courtesy of Prof. Duncan Huron, Duke Univ.

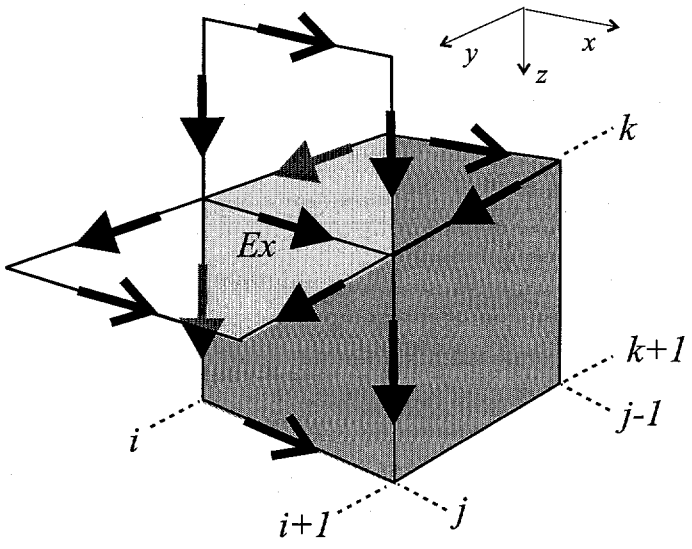

Figure 2. Representation of the staggered grid stencil used for the FD computations. Discretization of the $\nabla \times \nabla \times$ operator for the $\hat{x}$–component of equation (5) at point $(i + \frac{1}{2}, j, k)$ utilizes components of $\mathbf{E}'$ from each of the 13 locations indicated by the arrows. A subset of 9 $\mathbf{E}'$–components, indicated by solid arrowheads, is used for discretization of the $\bar{\sigma}\mathbf{E}'$ term. Also shown is a model cell throughout which the electrical conductivity tensor $\bar{\sigma}_{i\,j-1\,k}$ remains constant. For notational convenience, we make the following definitions: $\Delta x_i = x_{i+1} - x_i$, $\Delta y_j = y_{j+1} - y_j$ and $\Delta z_k = z_{k+1} - z_k$.

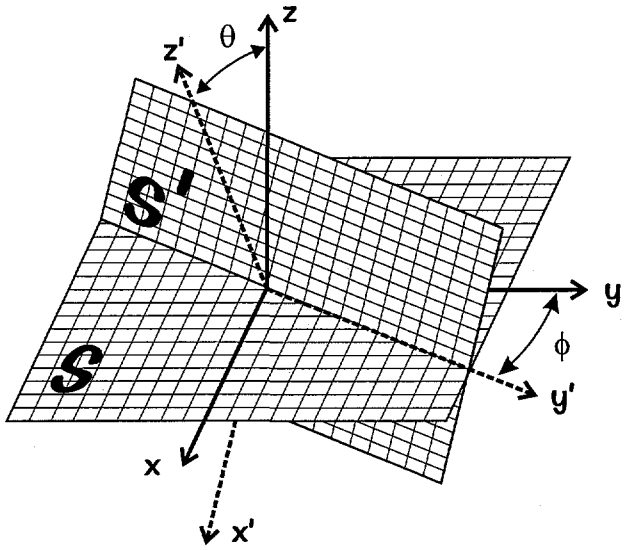

Figure 3. Geometric relationship between the model reference frame (x, y, z) and the principal axes reference frame (x', y', z'). The plane labeled S intersects the origin and is perpendicular to the z axis. The plane labeled S', representing the bedding planes, intersects the origin and is perpendicular to the z' axis. Angles ϕ and θ represent the 'strike' and 'dip' of the plane S' with respect to the plane S.

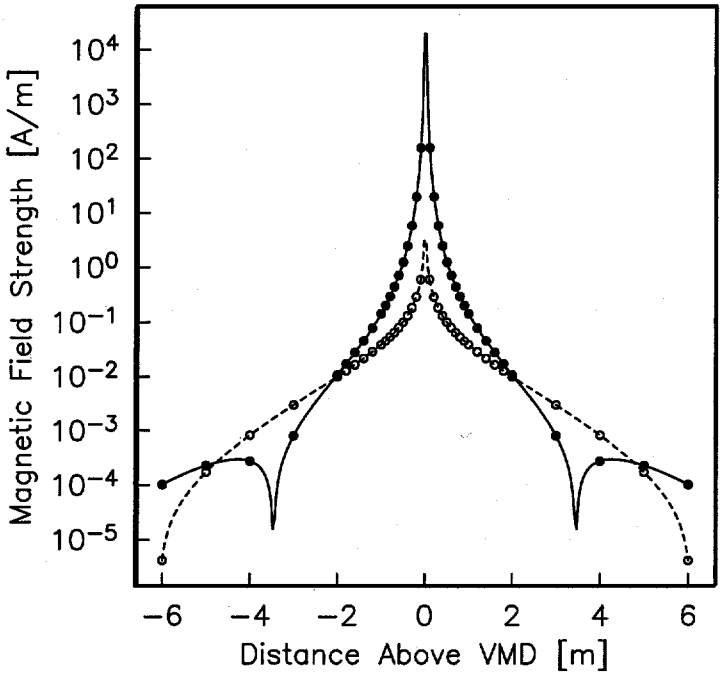

Figure 4. Comparison of analytic (lines) and FD (symbols) of the axial magnetic field magnitude due to a 100 kHz vertical magnetic dipole embedded in an anisotropic wholespace. Vertical and horizontal conductivities of the wholespace are 0.1 and 1.0 S/m, respectively. Open symbols and dashed lines represent the imaginary component of the field while closed symbols and solid lines represent the real component.

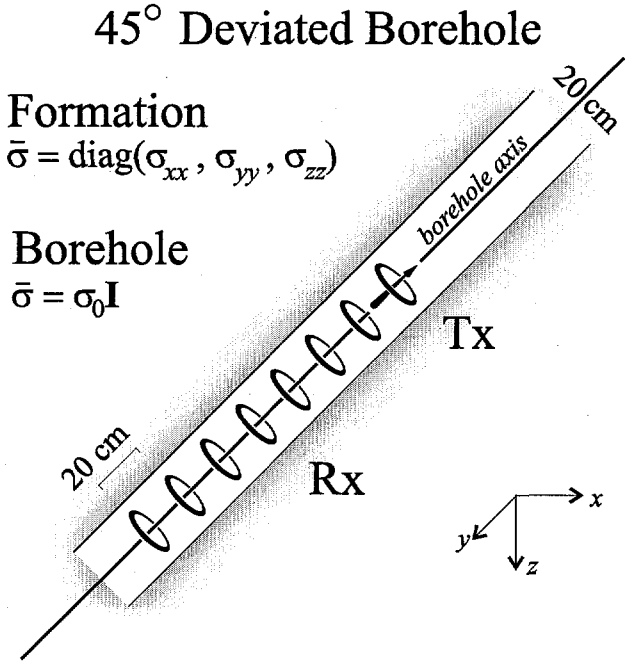

Figure 5. Schematic representation of a deviated borehole in an anistopic formation. The 45° deviation is constrained to the xz–plane. The transmitter (Tx) and receiver array (Rx) are coaxial loops centered on the borehole axis and each separated by 0.2m. Borehole conductivity is $\sigma_0 = 10\mathrm{S/m}$. Anisotropic formation conductivities are $\sigma_{xx} = \sigma_{yy} = 1.0\mathrm{S/m}$ and $\sigma_{zz} = 0.25$ S/m.

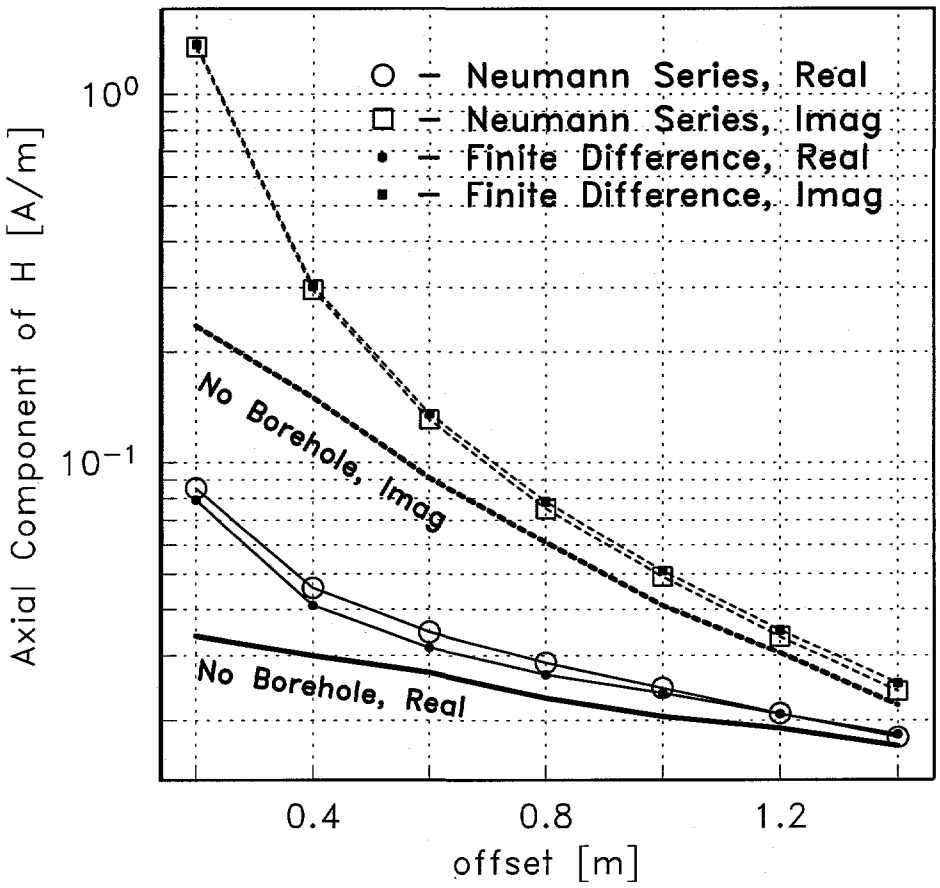

Figure 6. Comparison of the magnetic field along the axis of a 45° dipping borehole due to an axially aligned 160 kHz magnetic dipole. Shown here is the difference between the total field and the field due to the same source located in vacuum.

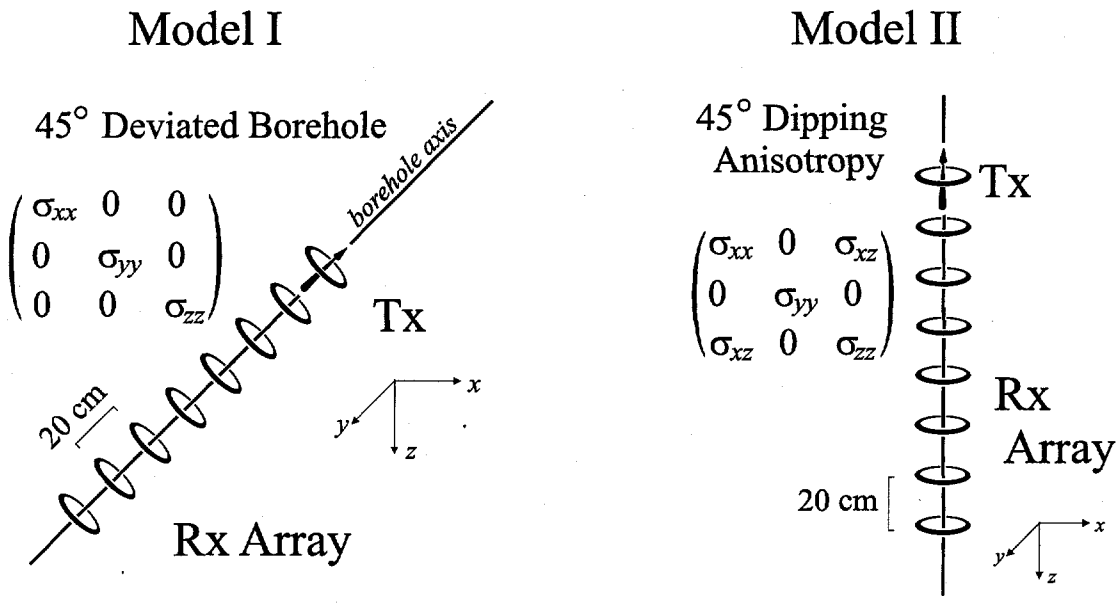

Figure 7. Schematic representation of two models constructed for an internal consistency check of the FD solution. Shown are the receiver (Rx) coil spacing, FD reference frame and formation conductivity tensor for each of the two models. The conductivity tensor of the formation is given by equation (11) where $\sigma_\perp = 0.1\text{S/m}$ and 1.0S/m. The transmitter (Tx) frequency is 100kHz.

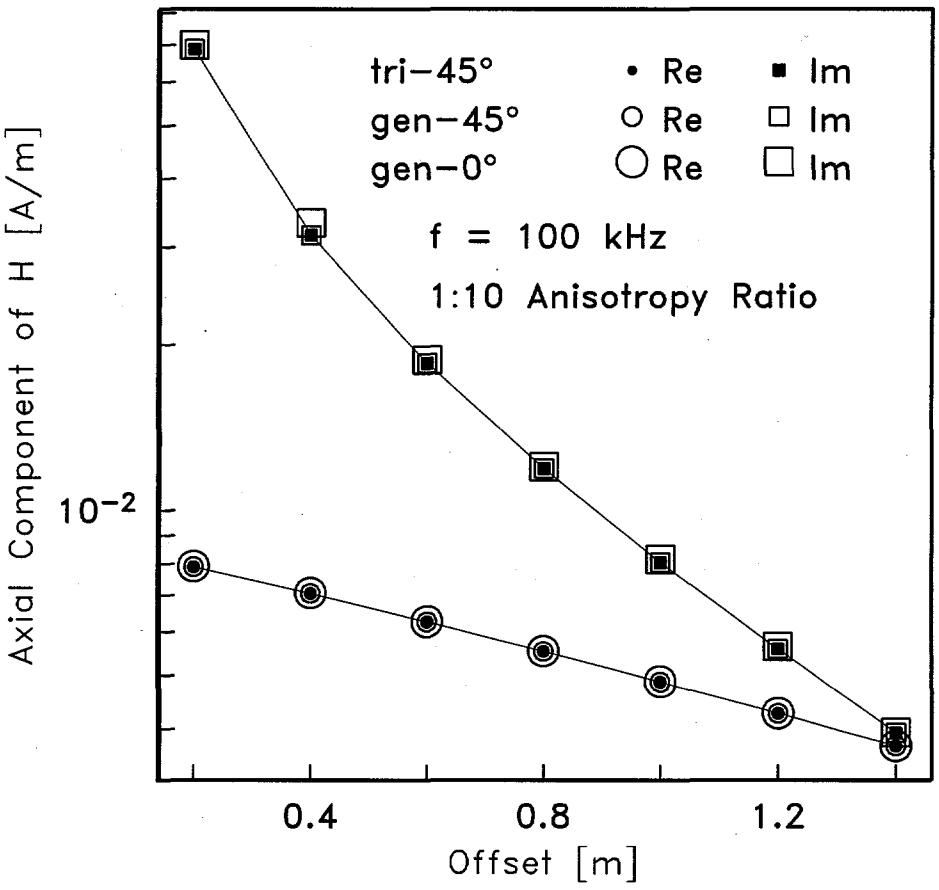

Figure 8. Axial component of the magnetic field FD results from evalution of the two models shown in figure 7. Shown here is the difference between the total field and the field due to the same source located in vacuum. Two solutions are presented for model I: one for a preliminary version of the FD code based on a strictly diagonal conductivity tensor (tri-45) and one which accepts a dense generalized conductivity tensor (gen-45). The FD solution for model II is shown by the symbols labeled (gen-0).

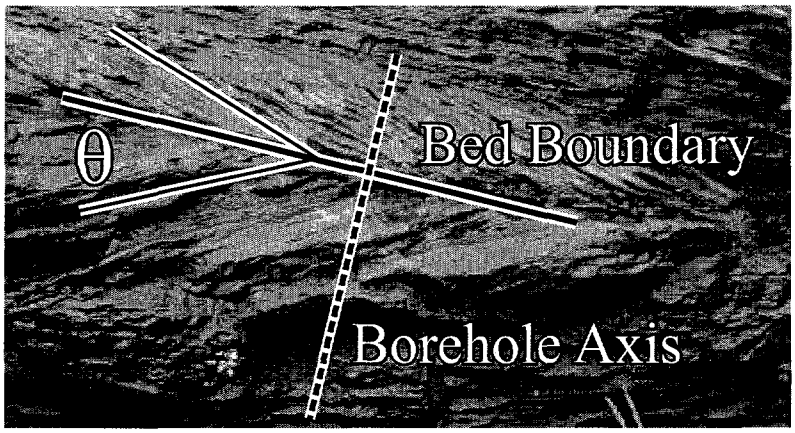

Figure 9. Photograph of a crossbedded sandstone with symmetric laminations dipping an angle θ with respect to the bed boundary. Also shown is the orientation of the borehole axis used in the numerical simulation of this structure. Photo courtesy of Prof. Duncan Huron, Duke Univ.

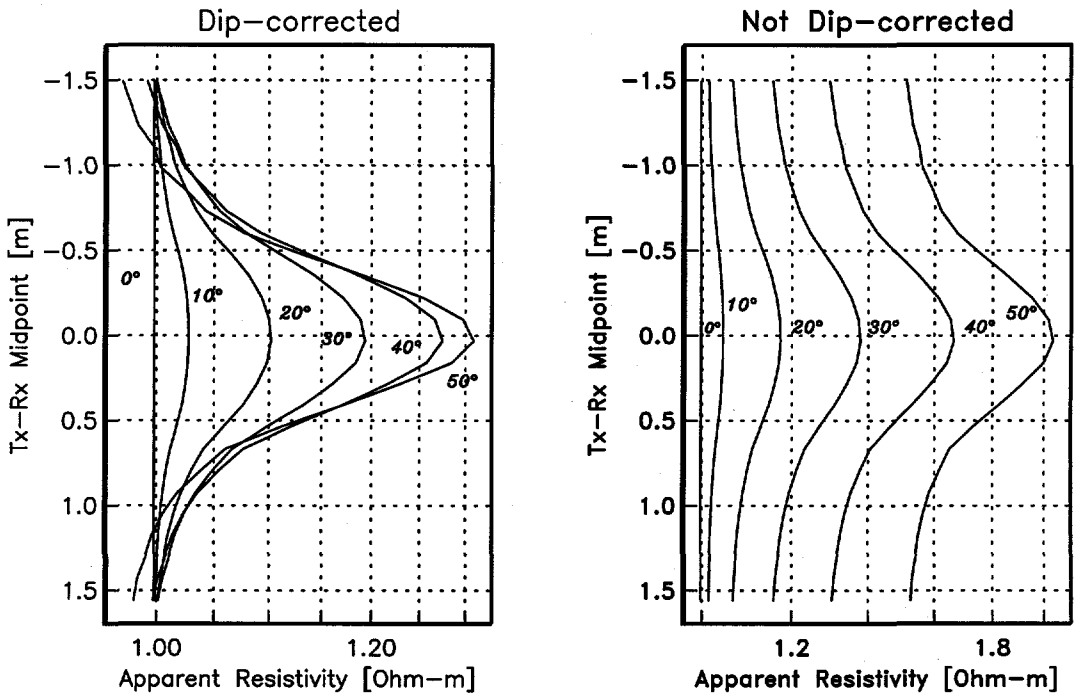

Figure 10. Apparent resistivity curves across a bed boundary in a symmetrically crossbedded formation (see Fig. 9). The bed boundary is located at 0.0 on the vertical axis. Shown are the results for six cases of symmetrically dipping laminae with θ ranging from 0° to 50°. The set of curves shown on the left have been scaled by a factor $\cos(\theta(z))$ where z is the midpoint between the transmitter (Tx) and receiver (Rx) coils. The unscaled apparent resistivity curves are shown on the right.

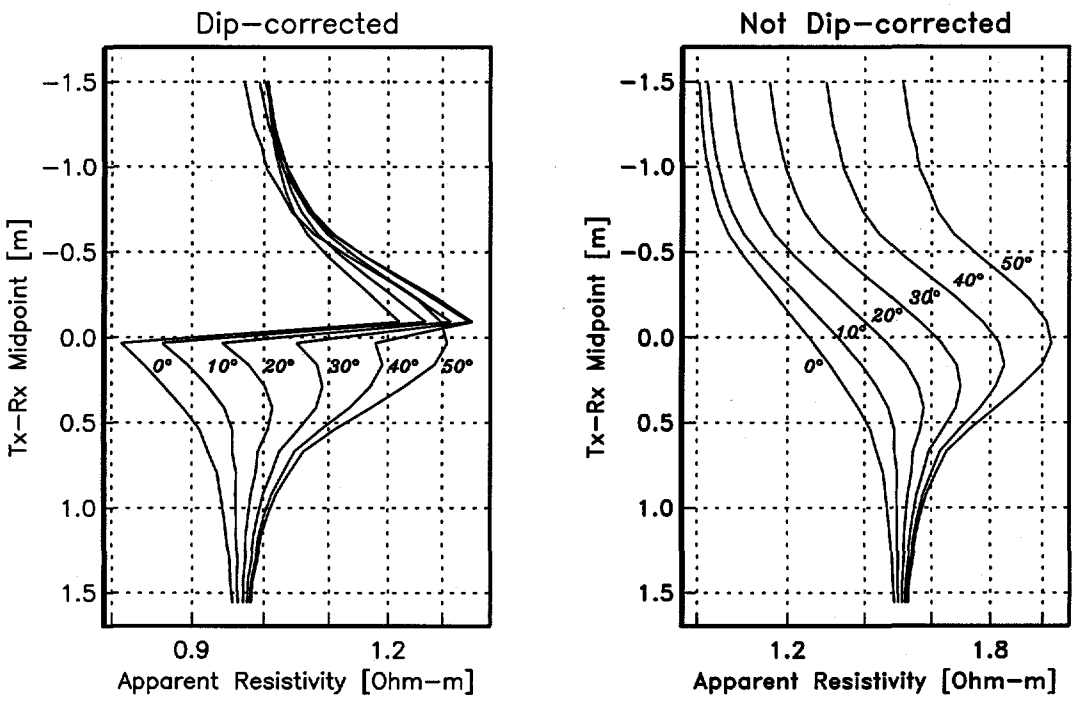

Figure 11. Apparent resistivity curves across a bed boundary in an asymmetrically crossbedded formation. The bed boundary is located at 0.0 on the vertical axis. Shown are the results for six cases where the orientation of the laminations in the lower bed remains fixed at 50° while the laminations in the upper bed vary by an angle $\theta = 0°, 10°, \ldots, 50°$. Note the presence of "polarization horns" at ~ 0.2 on the vertical axis. The set of curves shown on the left have been scaled by a factor $\cos(\theta(z))$ where z is the midpoint between the transmitter (Tx) and receiver (Rx) coils. The unscaled apparent resistivity curves are shown on the right.